

# Geometric Integration Over Irregular Domains with topologic Guarantees

Christian Engwer\*      Andreas Nüßing \*

February 28, 2022

## Abstract

Implicitly described domains are a well established tool in the simulation of time dependent problems, e.g. using level-set methods. In order to solve partial differential equations on such domains, a range of numerical methods was developed, e.g. the Immersed Boundary method, Unfitted Finite Element or Unfitted discontinuous Galerkin methods, eXtended or Generalised Finite Element methods, just to name a few. Many of these methods involve integration over cut-cells or their boundaries, as they are described by sub-domains of the original level-set mesh.

We present a new algorithm to geometrically evaluate the integrals over domains described by a first-order, conforming level-set function. The integration is based on a polyhedral reconstruction of the implicit geometry, following the concepts of the Marching Cubes algorithm. The algorithm preserves various topological properties of the implicit geometry in its polyhedral reconstruction, making it suitable for Finite Element computations. Numerical experiments show second order accuracy of the integration.

An implementation of the algorithm is available as free software, which allows for an easy incorporation into other projects. The software is in productive use within the DUNE framework [3].

## 1 Introduction

When dealing with partial differential equations (PDEs), methods using implicitly described domains have established themselves as an alternative to the traditional workflow using geometry adapted meshes. These methods usually solve the PDE on a larger domain and the actual geometry information is incorporated later on. Some popular methods are the Immersed Boundary method [18], Unfitted Finite Element [2] or Unfitted discontinuous Galerkin methods [5], eXtended [7] or Generalised Finite Element methods [19].

---

\*Institute for Computational und Applied Mathematics Einsteinstraße 62, 48149 Münster, Germany; {christian.engwer, andreas.nuessing}@uni-muenster.de

One popular class of implicit domain descriptions is via a scalar function, usually a so called level-set function [17] or a phase-field function [11]. These approaches are particularly attractive, as they can easily describe moving domains and even topology changes. In the following we have only very few requirements on the implicit description. A domain  $\Omega \subset \mathbb{R}^d$  is described using a continuous scalar function  $\Phi : \hat{\Omega} \subset \mathbb{R}^d \rightarrow \mathbb{R}$  such that:

$$\Phi(x) \begin{cases} < 0 & , \text{ if } x \in \Omega \\ = 0 & , \text{ if } x \in \partial\Omega \\ > 0 & , \text{ else.} \end{cases} \quad (1)$$

In order to incorporate the geometry information into the discretization, many of the aforementioned methods must integrate a function over the domain, or the surface. In order to evaluate these integrals, a discretized representation of  $\Omega$ , or  $\partial\Omega$ , is needed.

An efficient algorithm to reconstruct the interface between  $\Omega$  and its complement is the *marching cubes* algorithm presented in [15]. It originates from the field of computer graphics and is used to visualize volume data on a structured hexahedral grid. For each grid element a case number can be generated based on the sign of  $\Phi$  at the cell vertices. This key is then used as an index into a look-up table where the triangulation of the interface for this specific configuration is stored. This algorithm can be applied straight forward to tetrahedra, known as *marching tetrahedra* and other geometries [8]. As the case for cubes is the most challenging one, as we will discuss later, we only consider cubes throughout this paper.

There are several cases where the interface can not be uniquely determined based only on the sign of  $\Phi$  at the corners. These ambiguities can be resolved as presented in [6] with the *marching cubes 33* algorithm. For each face being ambiguous it is checked if two diagonally opposing vertices are connected over the face. In addition, a test needs to be performed, if two vertices could be connected through the element. For each case, the set of necessary tests is stored in a table. The resulting triangulation of the interface is topologically correct. An implementation and completion of this algorithm has been published in [14]. As we will discuss later, also this implementation lacks support for some special cases in 3D, where the topology is not properly retained.

A method which uses this idea for geometric integration over irregular domains has been presented in [16]. First cubes are triangulated into simplices independent of  $\Phi$ . To these simplices, a marching cubes type algorithm is applied to obtain a discrete representation of  $\Omega$  which is then used for integration. Using only simplices has the benefit that the amount of possible triangulation cases is significantly reduced. The downside is that the multilinear level-set is projected onto a linear level-set, resulting in a systematic distortion of the reconstruction along the newly introduced diagonals of cubes. Even with a symmetric criss-cross triangulation, these systematic error can not be avoided completely.

In this paper we employ the marching cubes ideas for geometric integration. We provide volume triangulations of the interior and exterior domain, along with the interface triangulation. These triangulations are topologically correct and consistent with each other. This allows for geometric integration over implicitly described domains. The

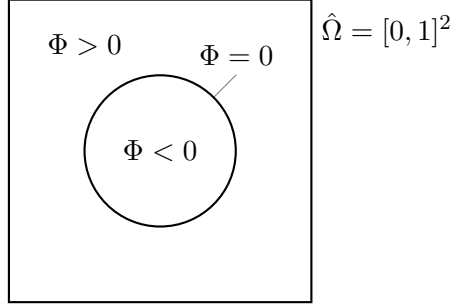


Figure 1: Illustration of level-set function  $\Phi(x) = \|x - (0.5, 0.5)^T\|_2 - 0.25$  on  $\hat{\Omega} = [0, 1]^2$

partitioning into interior and exterior of each element's face based on the volume triangulation is consistent with the triangulation which results from the application of the lower dimensional algorithm to the face. Although we only discuss the case of hexahedral elements, the algorithm is implemented for different dimensions and element types.

In the next section we introduce mathematical preliminaries and discuss the required consistencies. Section 3 elaborates the existing approaches, which were already briefly mentioned in the introduction. The major contribution of this paper is the presentation of a *topology preserving marching cubes* (TPMC) construction in Section 4, where we also compare the results of our new approach to the existing ones for chosen typical pathologic cases. The method is implemented as a C++ library, using python for automatic code generation as discussed in Section 5. Finally, in Section 6 numerical experiments are presented which verify the accuracy and the topologic consistency for the TPMC algorithm.

## 2 Preliminaries

### 2.1 Implicitly described domains

Let  $\hat{\Omega} \subset \mathbb{R}^d$  denote a polygonal outer domain of dimension  $d \in \mathbb{N}$ . A subdomain  $\Omega \subset \hat{\Omega} \subset \mathbb{R}^d$  is described using a level-set function  $\Phi$ , see (1), like illustrated in Figure 1.

The boundary  $\partial\Omega$  corresponds to the zero level-set  $\Phi^{-1}(0) := \{x \in \hat{\Omega} \mid \Phi(x) = 0\}$ . We call  $\partial\Omega$  the interface. Without loss of generality we restrict the threshold value to 0. A level-set function with an arbitrary threshold  $\alpha \in \mathbb{R}$  can be obtained by using  $\tilde{\Phi}(x) := \Phi(x) - \alpha$ .

Note that it is also possible to describe the motion of a moving interface from an Eulerian point of view in terms of a level-set function and an associated PDE, where  $\Phi(x, t)$  satisfies the level-set advection equation

$$\Phi_t + \mathbf{v} \cdot \nabla \Phi = 0 \quad \text{in } \hat{\Omega},$$

where  $\mathbf{v}(x, t)$  is a velocity field corresponding to the evolution of  $\Omega$  and  $\Gamma$ .

In practice the level-set is given as a discrete scalar function  $\Phi_h$ . A common choice is to use a conforming first order discretization, which is also assumed in this paper.

We consider a mesh  $\mathcal{M}(\hat{\Omega})$ , which is a discretization of the domain  $\hat{\Omega} \subset \mathbb{R}^d$ . The following properties hold:  $\mathcal{M}(\hat{\Omega}) = \{E_i | i \in \{0, \dots, N-1\}\}$  forms a partition of  $\hat{\Omega}$  with  $E_i \cap E_j = \emptyset$  if  $i \neq j$  and  $\bigcup_i \bar{E}_i = \hat{\Omega}$ .  $E_i$  denotes the codimension 0 elements of  $\mathcal{M}$ , i.e. the mesh cells. In 3D we only consider meshes with cubes, simplices, prisms and pyramids. In many cases a mesh consists either of cubes or simplices. In 2D only cubes and simplices are considered.

Apart from mesh cells we identify the following sub entities of  $\mathcal{M}$ : faces  $\gamma$  (codimension 1), edges  $\kappa$  (codimension  $d-1$ ) and vertices  $\xi$  (codimension  $d$ ). When looking at the codimension it becomes obvious, that in 2D faces and edges are the same. We still want to distinguish these to avoid confusion, when it comes to generalizations of the algorithm. For a formal definition of the grid and its properties, as we consider it, we refer to [4].

The discrete level-set is given as a scalar, continuous and piecewise multi-linear function. We choose a representation using vertex values. As  $\Phi_h$  is linear along edges  $\kappa_i$  it can be written as:

$$\Phi_h(\xi_0 + t(\xi_1 - \xi_0)) = \Phi_h(\xi_0) + t\Phi_h(\xi_1) ,$$

with  $\xi_0$  and  $\xi_1$  denoting the vertices associated with  $\kappa_i$ .

## 2.2 Numerical integration over implicitly described domains

The aim of the presented algorithm is to compute the integral of a function  $f : \hat{\Omega} \rightarrow \mathbb{R}$  over the domain  $\Omega$  described by a discrete level-set function  $\Phi_h$ . In the following discussion geometry described by  $\Phi_h$  is considered the exact geometry. The integration over the domain boundary  $\partial\Omega$  or the complement  $\hat{\Omega} \setminus \bar{\Omega}$  can be done in a similar manner. Using a triangulation  $\mathcal{M}(\hat{\Omega})$  of  $\hat{\Omega}$ , we compute a sub-triangulation  $\{E_i^j\}$  of the intersection of each element  $E_i$  and  $\Omega$ .

$$\begin{aligned} \int_{\{\Phi < 0\}} f dx &= \sum_i \int_{E_i \cap \{\Phi < 0\}} f dx \\ &\approx \sum_i \int_{E_i \cap \{\Phi_h < 0\}} f dx \\ &\approx \sum_i \sum_j \int_{E_i^j} f dx \end{aligned}$$

The first approximation is unavoidable, the approximation in the last step is due to our numerical integration and is subject of the discussion in the section. The integration over a simple element  $E$  (e.g. a simplex or cube) can be done on its reference element using a common quadrature rule:

$$\int_E f dx = \sum_k f(T_E(q_k)) w_k | \det(J_{T_E}(q_k)) |$$

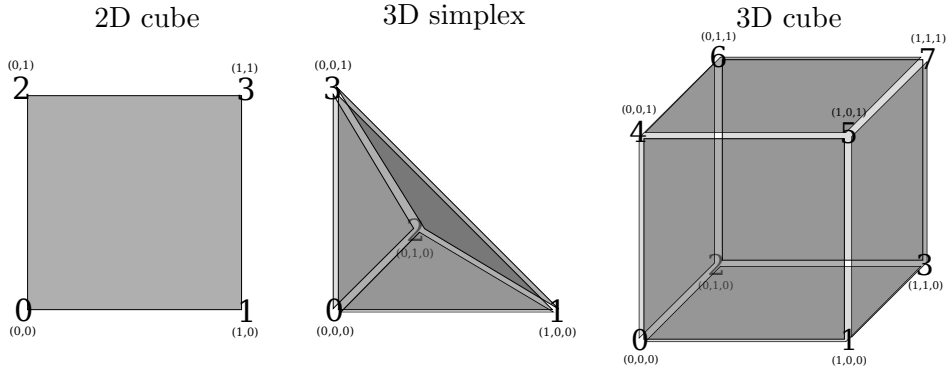


Figure 2: Vertex numbering and positions in the reference elements.

Here,  $T_E$  denotes a bijective map between  $E$  and its reference element and  $J_{T_E}$  denotes its Jacobian. In the literature different choices of reference elements are considered. We follow the definition used by the DUNE project. A list of these reference elements is given in Figure 2.

### 2.3 Topological guarantees

In order to allow the algorithm to be employed in a wide range of different methods, we demand that a sub-triangulation fulfills certain topological guarantees.

1. The connectivity pattern of the cell vertices must be preserved within each subentity. In particular this means that vertices connected along an edge, face or volume, should still be connected via the same subentity.
2. This requirement is related to the previous point. The curved interface  $\partial\Omega \equiv \Phi_h^{-1}(0)$  partitions each grid cell into patches belonging to either  $\Omega$  or the complement  $\hat{\Omega} \setminus \Omega$ . We require that the number of patches and their domain association is preserved for the polygonal reconstruction.
3. The vertices of the reconstructed interface lie on the exact zero level-set (of the discrete level-set function), i.e. for each vertex  $\xi_i$  the property

$$\Phi_h(\xi_i) = 0$$

holds.

## 3 Existing approaches

In this section we discuss existing approaches for computing a polygonal reconstruction of the interface  $\partial\Omega$  on hexahedral meshes. Extensions to other element types and other dimensions are always possible.

A well known algorithm is the marching cubes algorithm [15]. In [5] we described how integration rules for  $\Omega$  can be constructed, following the ideas of the marching cubes algorithm. In the following we refer to this algorithm as *MC*. The general idea is to only consider the sign of the function values in the vertices. Depending on these values  $2^{2^{\text{dim}}}$  different configuration can be distinguished, which can be reduced to 15 basic cases in 3D by taking rotation and mirroring into account. This allows to quickly reconstruct the interface using predefined rules.

A similar approach was presented in [16], where the authors basically propose integration rules constructed similar to marching tetrahedrons [13]; cubes are split into simplices using the Kuhn triangulation [12] and then tetrahedra are triangulated based on their vertex values. In the following we refer to this algorithm as *K/MT*.

As described in different publications, the classic marching cubes algorithm is not able to preserve the topology of the original iso-surface. [6] describes how in the marching cubes 33 additional evaluations in the face or volume help to resolve those ambiguities. A full implementation was published in [14]. In the following we refer to this algorithm as *MC33*. None of the existing approaches can fulfill all of the afore described topological guarantees.

While the first property is not fulfilled by the classic *MC* algorithm, the *MC33* algorithm describes an approach, which guarantees this consistency, at least for most cases. In Section 4 we will describe the cases where the *MC33* reconstruction is not sufficient. The *K/MT* algorithm on the other hand seems to solve the problem of such ambiguities, as the reconstruction on a simplex is always unique. The reconstruction is unique, but in general not correct, as the algorithm implicitly chooses one solution, due to the previous Kuhn triangulation and by this introduces a preferential direction.

Difficulties arise regarding the third property, which is fulfilled by neither the *MC33* algorithm, nor the *K/MT* approach. In the case of *MC33*, nodes in the cube are introduced as weighted averages of the position of cell vertices to describe a reconstruction in certain special cases. Such cases can not arise in 2D, but only in 3D. Using these nodes in the polygonal reconstruction of the interface  $\partial\Omega$ , is sufficient from a visualization point of view, but not for simulation purposes, as in general the nodes do not lie on the interface. Depending on the numerical algorithm and the model this can lead to systematic errors, e.g. in a curvature reconstruction.

The *K/MT* algorithm first applies a simplex triangulation. On each simplex, the level-set function is assumed to be linear, which is not correct, as it is actually bi-linear in 2D or tri-linear in 3D. This leads to reconstructed points, which are slightly off the interface. In addition, the triangulation into simplices introduces an anisotropy in the reconstructed interface, see Figure 4.

Further examples of violated consistencies are shown in Section 4.2, where we will also discuss how to prevent these problems using the proposed *TPMC* algorithm.

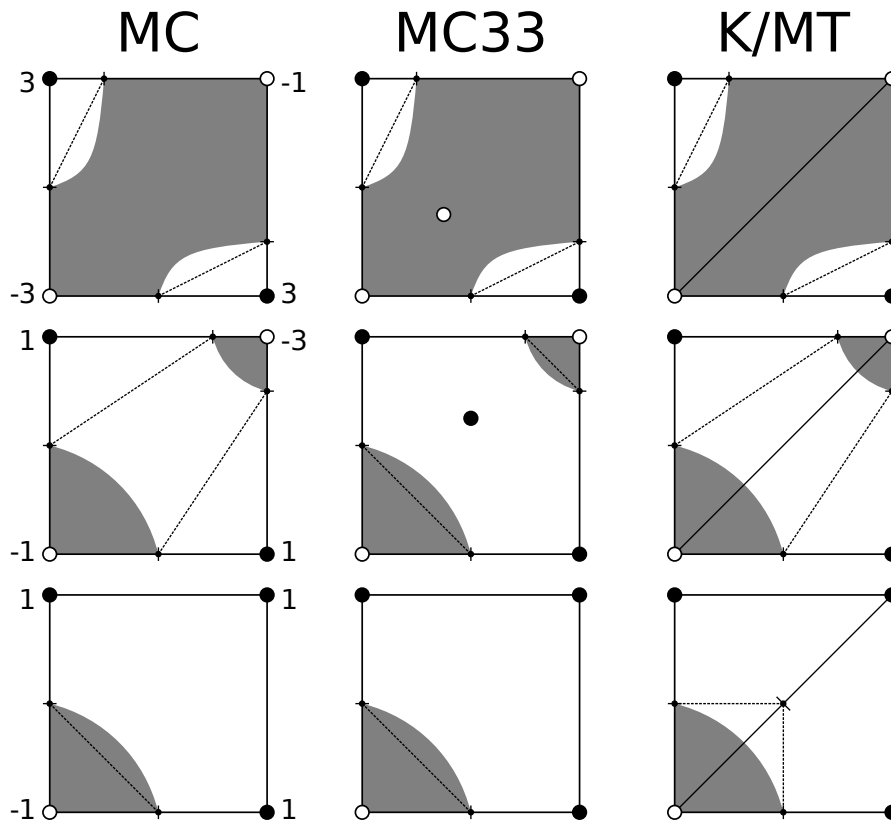


Figure 3: Comparing the existing algorithms: Problems in maintaining the topology for the reconstructed interface. Gray area: original sub-domain. Dots: reconstruction points (black: outside, white: inside). Dashed line: reconstructed interface.

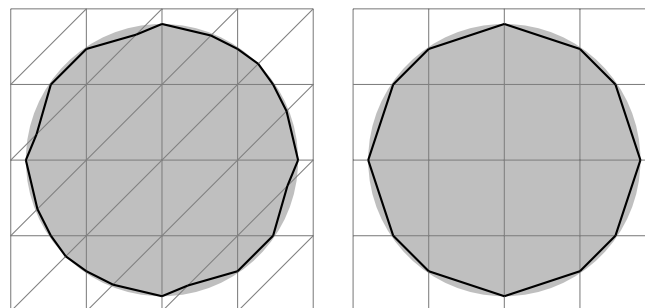


Figure 4: reconstructed interface of a circle using the K/MT approach (left) and MC33 (right)

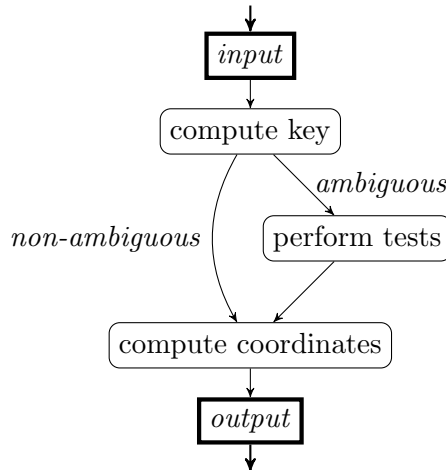


Figure 5: structure of the general algorithm for the generation of a sub-triangulation

## 4 Algorithm

In the following section, we will describe the algorithm for computing the sub-triangulation of a single grid cell using the vertex values of the level-set function. All computations can be performed on the reference element in cell local coordinates.

### 4.1 General Idea

The main idea is to map a set of corner values to a table-index. The index gives access to different tables which store precomputed general triangulations of the interior, exterior and interface of  $\Omega$ . Based on this general triangulation we can compute the actual triangulation by incorporating the corner values. The basic algorithmic structure is sketched in Figure 5.

The generation of the table index is subdivided into two steps: the computation of a key and, if necessary, the application of certain tests if the key is ambiguous. The key of a sequence of corner values  $(v_0, \dots, v_{n-1})$  of  $\Phi_h$  is defined as

$$\text{key}(v_0, \dots, v_{n-1}) := \sum_{i=0}^{n-1} \chi_{\mathbb{R} \geq 0}(v_i) 2^i,$$

where  $\chi_M$  denotes the indicator function

$$\chi_M(x) := \begin{cases} 1 & , x \in M \\ 0 & , x \notin M \end{cases}.$$

An example for the key computation on a two dimensional square is shown in Figure 6. For some cases, this key describes the topology completely. Other cases require



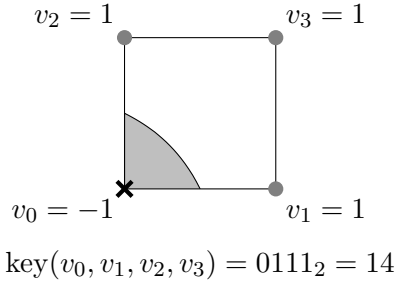


Figure 6: generation of the key for a two dimensional square domain based on the level set values in the corners

additional tests to determine the triangulation. We distinguish between two types of tests: face tests and center tests.

The triangulation of a quadratic face is ambiguous, if diagonally opposing vertices have the same and neighboring vertices a different sign. For such a case, a test needs to be performed to decide if the face center is in  $\Omega$  or  $\hat{\Omega} \setminus \bar{\Omega}$ . The interface on the ambiguous face builds a hyperbola. An example for such an interface can be seen in Figure 7. The sign of the face center is given as the sign of the hyperbolas center. For vertex values  $A, B, C, D$  at vertices 0, 1, 2, 3 respectively, the center is located (in local coordinates of the face) at

$$(c_x, c_y) := \left( \frac{A - C}{A - B - C + D}, \frac{A - B}{A - B - C + D} \right).$$

and its sign can be computed as

$$\text{sgn}(A) \text{sgn}(AD - BC).$$

For further details, we refer to [6]. In three space dimensions further ambiguities can occur.

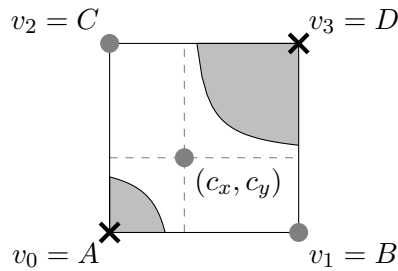


Figure 7: Interface of an ambiguous case on a quadratic face.  $v_0$  and  $v_3$  are negative and  $v_1$  and  $v_2$  are positive. The interface forms a hyperbola with its center located at  $(c_x, c_y)$ .

Vertices which are not connected via a face can still be connected through the volume. This means that the iso-surface forms a kind of tube through the element. A method to test this has been presented in [6] which we will recall here. Let  $v$  and  $w$  denote two vertices on opposite ends of a diagonal of the cube which have the same sign and are not connected via a set of faces. If and only if  $v$  and  $w$  are connected through the cubes volume, there exists a plane parallel to a face on which the projections of  $v$  and  $w$  are connected. This connection can be explicitly calculated in terms of the cubes vertex values. Let  $A_0, B_0, C_0$  and  $D_0$  denote the values at the vertices of the face containing  $v$  and  $A_1, B_1, C_1$  and  $D_1$  denote the values at the vertices of the face containing  $w$ , while  $A_0$  denotes the value at  $v$  and  $D_1$  denotes the value at  $w$ . We assume that  $A_0$  and  $D_1$  have a positive sign. The value along an edge perpendicular to the two faces is given by the linear functions  $A_t, B_t, C_t, D_t$  for  $t \in [0, 1]$ . To calculate the connection, we consider the following quadratic function

$$p : [0, 1] \rightarrow \mathbb{R}; t \mapsto A_t D_t - B_t C_t = at^2 + bt + c, \quad (2)$$

where the coefficients  $a, b, c \in \mathbb{R}$  are given by

$$\begin{aligned} a &= (A_1 - A_0)(D_1 - D_0) - (C_1 - C_0)(B_1 - B_0) \\ b &= D_0(A_1 - A_0) + A_0(D_1 - D_0) - B_0(C_1 - C_0) - C_0(B_1 - B_0) \\ c &= A_0 D_0 - B_0 C_0 \end{aligned}$$

The value of  $p$  corresponds to the value of the center of the hyperbola on the given plane. The positive areas are connected, if  $p$  has a maximum at  $t_{\max} \in [0, 1]$  with  $p(t_{\max}) > 0$  and the values  $A_t, B_t, C_t, D_t$  have the correct sign. Otherwise they are separated. Again, we refer to [6] for a detailed description.

The necessary tests for a specific case form a tree structure, which is traversed in order to calculate the table index. A table containing the necessary tests is available in an online resource of [14]. Note though, that we found two tests to be missing: for cases 10 and 12 with positive tests for both ambiguous faces, one has to check whether the exterior vertices are connected through the cube.

Once the table index has been computed, it can be used to retrieve general triangulations. Such a triangulation describes its local elements using the vertex numbering of the reference element. The actual coordinates are computed using the vertex values. We distinguish between five types of vertices which are described in Section 4.3.

## 4.2 Additional consistencies

As noted in Section 2 additional consistencies are required to ensure the topological guarantees. The MC33 improves the classical MC algorithm to ensure topological consistency for the reconstructed interface. While this is sufficient for visualization, it is in general not sufficient for numerical simulations.

We want to illustrate the issue with a concrete example. Figure 8 shows on the left the correct interface of a tri-linear function with vertex values as listed in table 1. After resolving the ambiguities the MC33 algorithm provides a reconstruction where parts of

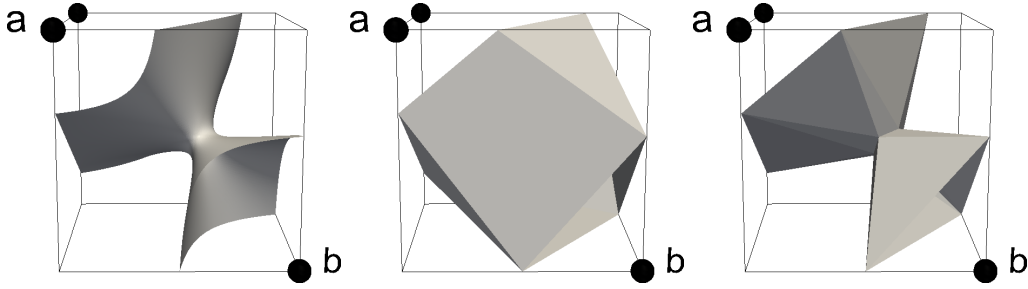


Figure 8: Violation of the topologic consistency in a face (front), using MC33 and the correct reconstruction using TPMC. Left: discrete level-set, center: reconstruction from MC33 (case 6.1.2 of [14]), right: TPMC reconstruction. For the choice of vertex values see Table 1.

Vtx	0	1	2	3	4	5	6	7
Pos	(0,0,0)	(0,0,1)	(0,1,0)	(0,1,1)	(1,0,0)	(1,0,1)	(1,1,0)	(1,1,1)
Value	-4	4	-1	-1	2	-3	5	-1

Table 1: Vertex values for the example illustrated in Figure 8.

the interface are not in the interior of the cell anymore, but are pushed into the frontal face of the cube; the volume which lies in-between vanishes when using the discrete level-set function. This leads to an unresolvable inconsistency between the trace of the volume reconstruction and a direct reconstruction in the cube face. Therefore, these reconstructions do not fulfill the topological guarantees and are not accurate enough for numerical purposes. This issue can be resolved, by adding interior points to reconstruct the interface and especially the vanishing volume more accurately.

### 4.3 Construction of Vertices

Based on the general reconstruction rule stored in the look-up table the actual reconstruction is computed. This requires the construction of vertices based on the actual vertex values. We distinguish between five types of vertices:

1. *original vertices*:

For the volume reconstruction we have to incorporate the vertices of the reference element, our implementation is based on a dimension independent numbering used in the DUNE framework (see Figure 2).

2. *edge vertices*:

These vertices describe the position of the interface along an edge of the reference element. As the level-set is linear along an edge the position is easily computed as weighted average

$$x_{\{A,B\}} = x_A \frac{B}{B-A} + x_B \frac{A}{A-B}$$

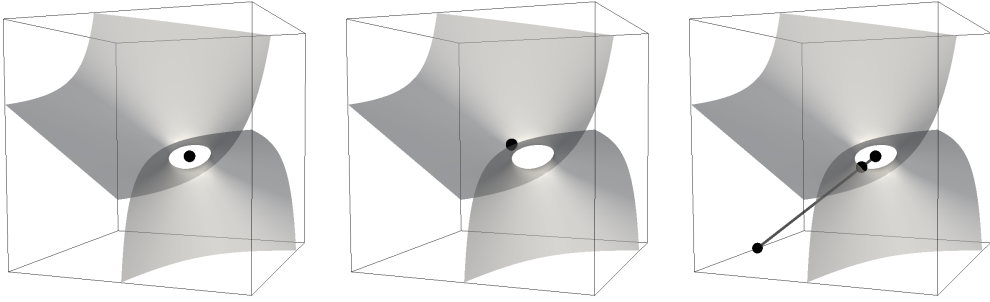


Figure 9: Maximum vertex (left), root vertex (center) and intersection vertex (right) for the basic case 6.1.2. For the choice of vertex values see Table 1.

where  $A, B$  denote the level-set values of the vertices at  $x_A, x_B$  of the edge.

In order to resolve the issues described in Section 4.2 we require additional vertices in the interior of the cell.

3. *maximum vertices:*

By maximum vertices we denote the vertices given by the maximum of the quadratic function  $p$  defined in equation (2) of the interior connectivity test. Such a vertex is located at the “center” of the constriction of a tube-like structure. For an example of such a structure see Figure 8 and an example of a maximum vertex see Figure 9. They are not used directly in the triangulation since they do not lie on the interface, but are used as helper vertices for vertices of type 5.

4. *root vertices:*

Root vertices are defined similar to maximum vertices and are given by the roots of the quadratic function  $p$  defined in equation (2). If the interior connectivity test is positive, there is a plane (defined by  $t_{\max}$ ) parallel to a given face of the cube where the restricted interface forms a hyperbola. Moving the plane along its normal and following the path of the center of the hyperbola, the root vertices are given by the intersection of the path with the interface. An example for a root vertex is shown in Figure 9. Note that such a point always exists as in this case the sign at the center of the hyperbola is known to change.

5. *interior vertices:*

These points are computed as the intersection between the iso-surface and an a-priori chosen line. As the line is not axis-aligned and the level-set function  $\Phi_h$  is tri-linear we can have up to three intersection points along the line. We compute all intersection simultaneously using the Aberth algorithm [1]. The latter is a Newton-type iterative method for finding the roots of a polynomial. It makes sure that no two approximations converge to the same roots.

**Example (Construction of interior; case 6.1.2)** *To illustrate the different steps of the algorithm, we consider the example illustrated in Figure 8. The according vertex values are listed in Table 1 and the vertex value yield the key  $01001010_2 = 82$ , which correspond to the basic case 6 (see [14]). This case is ambiguous as vertices 1 and 6, which are connected via a diagonal through the cube, have the same sign and are not connected over faces of the cube. To perform the corresponding test, we compute the coefficients of the quadratic function with respect to the front face, which is given as*

$$p(t) = -42t^2 + 37t - 8$$

*This function has a maximum at  $t_{\max} = 7/84 \in [0, 1]$  and  $p(t_{\max}) = 5/168 > 0$ . The values of the projections are  $A_{t_{\max}} = 1/12$ ,  $B_{t_{\max}} = -1$ ,  $C_{t_{\max}} = -9/14$  and  $D_{t_{\max}} = 3/14$ . These values show, that in the plane of  $t_{\max}$ ,  $A_0$  and  $D_1$  are connected. This result corresponds to the basic case 6.1.2.*

*For this basic case we query the look-up tables and obtain reconstruction rules for interior, exterior and interface, which describes a set of parts as a list of vertices and a list of elements/faces. These describe primitive geometric objects, suitable for numerical integration. In our implementation the reconstruction of the interior, exterior and interface contain lists of 23, 21 and 15 parts respectively. The vertices in these lists are encoded via their associated subentity in the reference element. The lists for the specific case 6.1.2 contain for example reference vertex 3, which is located at  $(1, 1, 0)$ . Another example is the intersection vertex between the reference vertices 1 (located at  $(1, 0, 0)$ ) and 3. This vertex is found by linear interpolation from the vertex values 4 and  $-1$  which gives  $(1, 4/5, 0)$ . A more complex example is the intersection vertex between the maximum vertex and the middle point on the edge of vertices 0 and 2 as shown in the right Figure 9. First, we compute the maximum vertex by computing the center of the hyperbola in the plane parallel to the front face at  $t_{\max} = 7/84$ . This vertex is given as approximately  $(0.61017, 0.45238, 0.44552)$  (see Figure 9 left). In general  $\Phi$  is locally a trilinear function, thus we use the Aberth-method to get the intersection with interface of the line between this maximum vertex and the center  $(0, 0.5, 0)$  of the edge between vertices 0 and 2. The intersection vertex is approximately  $(0.54437, 0.45752, 0.39748)$ . We compute the vertex position for each vertex in the list by the methods defined above. From these vertices we can construct the volume of the interior and exterior as the union of the respective parts.*

## 5 Implementation

An implementation of the algorithm is available via `python-pip`, all tests performed in this paper are available for download from ZENODO [10]. A python library contains a list of all basic cases and their associated information. From the basic cases the python code computes the full list and can then generate C++ code. This generated code only uses standard C++ components and can easily be used in other projects. The code is in productive use in DUNE for our implementation of the Unfitted Dicontinuous Galerkin method [9].

The C++ library stores all information in a set of different look-up tables. The tests are stored as binary trees in breadth-first order as an implicit data structure in arrays. The library provides a basic interface to perform the tests and export geometric reconstructions as sets of sets of vertices. The library is templated, so that it can work with user defined container types and coordinate types. This allows to incorporate it into existing projects, without having to change internal data structures. As the look-up tables are stored as plain C arrays, they can also be incorporated into C or Fortran applications.

## 5.1 Look-up tables

The geometric information of the sub-triangulation parts for each case is stored in three different tables:

1. Reconstruction of the interface  $\Gamma$
2. Reconstruction of  $\Omega$
3. Reconstruction of the complement of  $\Omega$

Note that we store two different tables for  $\Omega$  and its complement. Naively a sub-triangulation of the complement  $\hat{\Omega} \setminus \Omega$  could be computed by simply inverting the sign of the level set function. However, the resulting triangulation of  $\hat{\Omega}$  will in general no longer form a partition, it might contain holes or overlapping parts. To avoid this, both sub-triangulations have to be constructed with a matching interface. The vertices of the parts are encoded using their position in the reference element. The ordering of the vertices of each interface part is done such that the normal vectors to  $\Gamma$  can be computed using the right hand rule, i.e. the direction of the normal vector of an interface part with vertices  $x_0, x_1, x_2, \dots$  is given by the cross product of the tangential axes:  $(x_1 - x_0) \times (x_2 - x_0)$ .

In addition to the general geometric information we store information about the connectivity pattern w.r.t. each sub-domain. For each sub-triangulation part and each vertex we store an index of the local connected component it belongs to. Using this information, the global connectivity pattern can be computed without geometric coordinate comparisons.

Look-up tables are provided for all primitive geometries up to dimension three, i.e. for lines, triangles, quadrilateral, tetrahedra, prisms, pyramids and hexahedra. Thus the library can be used with a broad range of discrete level-set representations.

## 5.2 Example

Following the sketch in Figure 5 we first compute a key based on given vertex values. If we encounter an ambiguous case, this involves a set of different tests, which are retrieved from a binary tree stored in table `table_cube3d_mc33_face_test_order`. In the next step we compute all internal vertices listed in; as these computations might be expensive, it is done in a separate step to avoid repetitive computation. The list of

---

**Algorithm 1** C++ user code to compute an interior domain decomposition, as described in Example .

---

```
1 // some necessary typedefs
2 static unsigned int dim = 3;
3 typedef std::array<double,dim> Coordinate;
4 // instantiate the algorithm and some additional
5 // structures
6 tpmc::MarchingCubes<double, dim, Coordinate> mc;
7 tpmc::GeometryType geometry = tpmc::cube;
8 std::vector<Coordinate> vertices;
9 vertices.reserve(mc.getMaximalVertexCount(geometry));
10 // describe the geometry
11 std::vector<double> vertex_values =
12     {-4.0, 4.0, -1.0, -1.0, 2.0, -3.0, 5.0, -1.0};
13 // compute the key
14 std::size_t key = mc.getKey(vertex_values.begin(),
15                             vertex_values.end());
16 // compute additional vertices and append them
17 mc.getVertices(vertex_values.begin(), vertex_values.end(),
18               key,
19               std::back_inserter(vertices)
20               );
21 // compute interior reconstruction and store them in
22 // decomposition
23 std::vector< std::vector<int> > decomposition;
24 mc.getElements(geometry, key, tpmc::InteriorDomain,
25               std::back_inserter(decomposition)
26               );
```

---

necessary vertices is stored in `table_cube3d_vertices`. As the last step, we retrieve the desired information, e.g. the reconstruction of the interior domain  $\Omega$ . In this particular example `table_cube3d_cases_offsets` yields offsets into a reconstruction table, e.g. `table_cube3dsym_codim_0_interior` for the interior domain.

The corresponding C++ user code to compute the construction described in Example is listed in Algorithm 1.

The decomposition of the interior domain is described as a cell-to-vertex map in the form  $C_i \rightarrow \{v_j\}$ . Each entry describes a primitive geometry. This map is stored in the decomposition variable. Given the vertex numbers of a cell the actual coordinates are obtained by a lookup in the vector of vertex coordinates, stored in `vertices`. This description follows the approach used in most mesh file formats.

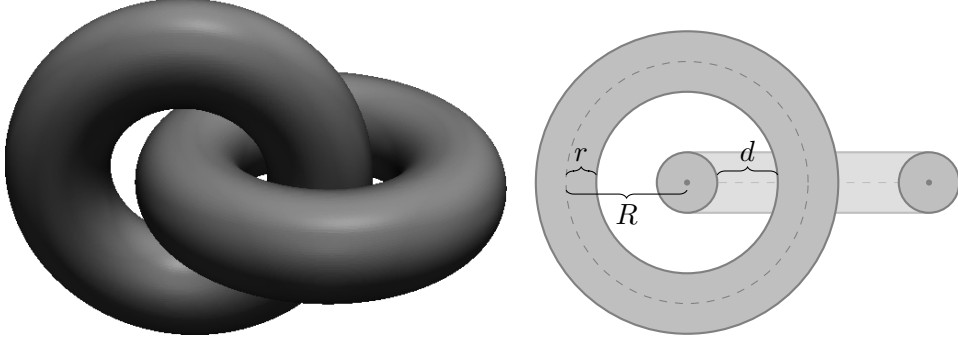


Figure 10: reconstructed interface of the test problem of two entangled tori and a cut along the hyperplane associated with one torus.

## 6 Evaluation

We present different numerical tests to evaluate the accuracy, the robustness and the efficiency of the proposed algorithm.

### 6.1 Surface Integral over two entangled Tori

To evaluate the convergence rate of the integration method, we use a test level-set function representing two tori. We set  $\hat{\Omega} = [0, 1]^3 \subset \mathbb{R}^3$  as the outer domain. For a unit vector  $n \in \mathbb{R}^3$  we define its associated hyperplane as  $H(n) := \{x \in \hat{\Omega} | \langle x, n \rangle = 0\}$ . The orthogonal projection onto  $H(n)$  is then given by  $P(n)(x) = x - \langle x, n \rangle n$ . The level-set function of a torus with radius  $R \in \mathbb{R}$  and tube radius  $r \in \mathbb{R}$  in a hyperplane  $H(n)$  is given by

$$\Phi_{R,r}(n)(x) := \sqrt{(\|P(n)(x)\| - R)^2 + \langle x, n \rangle^2} - r .$$

For  $\phi \in [0, \pi)$ , we set

$$n_1(\phi) := \begin{pmatrix} \cos(\phi) \\ \sin(\phi) \\ 0 \end{pmatrix}, \quad n_2(\phi) := \begin{pmatrix} -\sin(\phi) \\ \cos(\phi) \\ 0 \end{pmatrix}, \quad n_3 := \begin{pmatrix} 0 \\ 0 \\ 1 \end{pmatrix}, \quad c := \begin{pmatrix} 0.5 \\ 0.5 \\ 0.5 \end{pmatrix}$$

and define the level-set function of two entangled tori (see Figure 10), centered at  $c$ :

$$\Phi_{R,r,\phi}(x) := \min \left( \Phi_{R,r}(n_1(\phi)) \left( x - c + \frac{R}{2} \cdot n_3 \right), \right. \\ \left. \Phi_{R,r}(n_2(\phi)) \left( x - c - \frac{R}{2} \cdot n_3 \right) \right) .$$

The surface area of the level-set  $\Phi_{R,r,\phi}$  can be computed analytically as

$$S(\Phi_{R,r,\phi}) := \int_{\Gamma_{R,r,\phi}} 1 ds = 8\pi^2 Rr$$



grid size	$\min(e_S)$	–	$\max(e_S)$	$\bar{e}_S$	$\pm \sigma_1$
16	0.0451	–	0.0509	0.046	$\pm 3.2\%$
32	0.0108	–	0.0114	0.0110	$\pm 1.8\%$
64	0.00266	–	0.00275	0.00270	$\pm 1.1\%$
128	0.0006672	–	0.00067563	0.0006738	$\pm 0.3\%$
256	0.0001674	–	0.0001686	0.0001681	$\pm 0.2\%$

Table 2: Relative error  $e_S$  of the surface of the two tori test problem computed with TPMC as compared to the analytic solution. The level-set is discretized on a three dimensional structured grid with rectangular element. For each grid size we generate 30 randomly shifted datasets

The surface of the reconstructed interface using a structured grid with diameter  $h$  is denoted by  $S_h(\Phi_{R,r,\phi})$ . The relative error of a reconstructed surface is defined as

$$e_S := \frac{|S(\Phi_{R,r,\phi}) - S_h(\Phi_{R,r,\phi})|}{S(\Phi_{R,r,\phi})}$$

We define  $d = R - 2r$  as the distance between the two tori. For  $d = 0$  the two tori touch and the topology changes, the aspect ratio  $R/r$  in this case is 2.

We set  $R = 0.25$  with a distance  $d = 0.1$ , i.e. we choose the minor radius  $r = \frac{R-d}{2} = 0.075$  and set  $\phi = 0$ . In order to investigate the robustness of the method to grid perturbation, we shift the center of the tori randomly by a maximum  $h$ . For each grid size, we generate 30 random datasets. The results of the relative surface error for different grid sizes are listed in Table 2.

We can observe a second order convergence rate, as it is expected for a polygonal approximation. In addition, the computation is robust with respect to grid perturbation, since the variance tends to zero as  $h$  is reduced.

## 6.2 Robustness to Rotation

For  $d \rightarrow 0$  the topology changes, as the two tori “merge”. In the discrete reconstruction this happens already for  $d > 0$ . In this test we compute, for different directions  $\phi$  of the two tori, the critical distance  $d_c$  at which the topology changes, i.e. the number of discrete connected components switches from three to two. In this test the grid size is fixed  $h = \frac{1}{64}$  and  $R = 0.25$ , as in the first test. For values of  $\phi \in [0, \pi)$  we modify the minor radius  $r = \frac{R-d}{2}$  to compute the critical distance  $d_c = x \cdot h$ , using a bisection method. Figure 11 shows the critical distance with (TPMC) and without (MC) ambiguity-resolution (smaller is better).

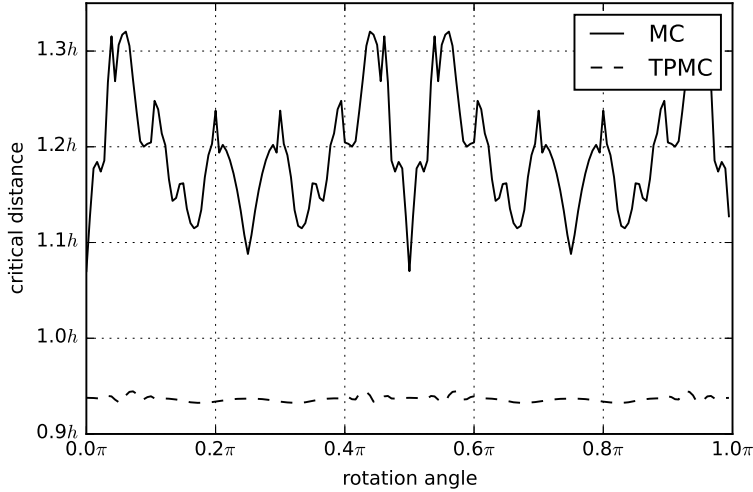


Figure 11: Two entangled tori are rotated in a three dimensional structured grid with rectangular elements. The distance between the tori is reduced and the distance at which the topology changes is noted in this figure as a multiple of  $h$ ; smaller is better. The solid line represents the data obtained by MC and the dashed one the data obtained by TPMC. MC is not robust with respect to the orientation of the tori.

For the method with ambiguity-resolution, the topology change occurs relatively stable at a distance below  $h$ , yielding a sub-voxel resolution. Without the ambiguity-resolution, meaning an anisotropic choice in an ambiguous case, the distance depends on the angle  $\phi$  and is overall above  $h$ .

### 6.3 Performance

In order to evaluate the performance overhead of TPMC as compared to MC, we generate pseudo-random values in  $[-1.0, 1.0]$  for each vertex of a three dimensional structured grid. We construct 30 data sets for each grid size and compute the unique key for each grid cell using TPMC and MC. For each data set, we average the time consumption over 30 iterations. We measure both the isolated time used for ambiguity resolution, and the total time consumption including the grid iteration.

This is a worst case scenario, as  $\Phi$  is usually a smooth function, so this test will encounter significantly more ambiguous case than an average application.

The resulting ratios between time for TPMC and MC can be seen in Table 3. The table also shows the number of face and center tests in relation to the number of key computations. We observe an increased time consumption of TPMC by a factor of approximately 2.2 for the ambiguity resolution, which can be expected due to the need for additional tests. For approximately three out of four key computations we need a face test and for two out of five we need a center test. When taking also the iteration over the

grid size	ambiguity resolution	total	test fraction	
	$\bar{T}_{\text{rel}} \pm \sigma_1$	$\bar{T}_{\text{rel}} \pm \sigma_1$	face	center
16	$2.27 \pm 2.07\%$	$1.23 \pm 2.57\%$	76.0%	22.0%
32	$2.20 \pm 1.24\%$	$1.18 \pm 0.48\%$	74.8%	21.8%
64	$2.17 \pm 0.72\%$	$1.17 \pm 0.25\%$	74.9%	21.8%
128	$2.18 \pm 0.64\%$	$1.17 \pm 0.34\%$	74.8%	21.8%
256	$2.19 \pm 1.86\%$	$1.18 \pm 0.50\%$	74.8%	21.8%

Table 3: Worst case test: Relative time consumption  $T_{\text{rel}} = T_{\text{TPMC}}/T_{\text{MC}}$  for TPMC as compared to MC on a three dimensional structured grid with  $N$  rectangular cells in each dimension. The timings are either the time used for ambiguity resolution or the total time, including grid iteration. We also show the fraction of tests involving face or center tests. For each grid size we compute 30 random datasets.

simple structured grid into account, the factor already reduces to approximately 1.18. We note that for a computationally more expensive grid iteration, for example using an unstructured grid, the factor will further decrease. As mentioned before, we want to point out that for smoother data, the need for additional tests is in general significantly smaller than for random data and therefore the performance overhead of the proposed method will significantly smaller.

## 7 Conclusion

We proposed a method for geometric integration over implicitly described domains. The method shows second order accuracy and a topologically correct representation of the geometry. The method is robust with respect to grid perturbation while imposing only a small performance overhead when compared to a non-correct algorithm. For an extension of the method to multiple level sets, one might consider a recursive application of the presented method. For such a purpose, the interpolation of the vertices has to be modified to take higher order edges into account.

## References

- [1] Oliver Aberth. Iteration methods for finding all zeros of a polynomial simultaneously. *Mathematics of Computation*, 27(122):pp. 339–344, 1973. [doi:10.1090/S0025-5718-1973-0329236-7](https://doi.org/10.1090/S0025-5718-1973-0329236-7).
- [2] John W. Barrett and Charles M. Elliott. Fitted and unfitted finite-element methods for elliptic equations with smooth interfaces. *IMA Journal of Numerical Analysis*, 7(3):283–300, 1987. [doi:10.1093/imanum/7.3.283](https://doi.org/10.1093/imanum/7.3.283).
- [3] P. Bastian, M. Blatt, A. Dedner, C. Engwer, R. Klöforn, R. Kornhuber,

- M. Ohlberger, and O. Sander. A generic grid interface for parallel and adaptive scientific computing. Part II: Implementation and tests in DUNE. *Computing*, 82(2–3):121–138, 7 2008. doi:[10.1007/s00607-008-0004-9](https://doi.org/10.1007/s00607-008-0004-9).
- [4] P. Bastian, M. Blatt, A. Dedner, C. Engwer, R. Klöfkorn, M. Ohlberger, and O. Sander. A generic grid interface for parallel and adaptive scientific computing. Part I: Abstract framework. *Computing*, 82(2):103–119, July 2008. doi:[10.1007/s00607-008-0003-x](https://doi.org/10.1007/s00607-008-0003-x).
- [5] P. Bastian and C. Engwer. An unfitted finite element method using discontinuous galerkin. *International Journal for Numerical Methods in Engineering*, 79(12):1557–1576, 2009. doi:[10.1002/nme.2631](https://doi.org/10.1002/nme.2631).
- [6] Evgeni V. Chernyaev. Marching cubes 33: Construction of topologically correct isosurfaces, December 17 1995.
- [7] J. Dolbow, N. Moes, and T. Belytschko. An extended finite element method for modeling crack growth with frictional contact. *Computer Methods in Applied Mechanics and Engineering*, 190(51-52):6825–6846, 2001. doi:[10.1016/S0045-7825\(01\)00260-2](https://doi.org/10.1016/S0045-7825(01)00260-2).
- [8] T Todd Elvins. A survey of algorithms for volume visualization. *ACM Siggraph Computer Graphics*, 26(3):194–201, 1992. doi:[10.1145/142413.142427](https://doi.org/10.1145/142413.142427).
- [9] Christian Engwer and Felix Heimann. Dune-udg: A cut-cell framework for unfitted discontinuous galerkin methods. In Andreas Dedner, Bernd Flemisch, and Robert Klöfkorn, editors, *Advances in DUNE*, pages 89–100. Springer, 2012. doi:[10.1007/978-3-642-28589-9\\_7](https://doi.org/10.1007/978-3-642-28589-9_7).
- [10] Christian Engwer and Andreas Nüßing. Tpmc examples and tests. ZENODO, 2015. doi: [10.5281/zenodo.44732](https://doi.org/10.5281/zenodo.44732). doi:[10.5281/zenodo.44732](https://doi.org/10.5281/zenodo.44732).
- [11] George J. Fix. Phase field methods for free boundary problems. Technical report, Department of Mathematical Sciences, Carnegie Mellon University, 1982.
- [12] H. Freudenthal. Simplicialzerlegungen von beschränkter Flachheit. *Annals of Mathematics*, 43:580–582, 1942. doi:[10.2307/1968813](https://doi.org/10.2307/1968813).
- [13] A. Guezic and R. Hummel. Exploiting triangulated surface extraction using tetrahedral decomposition. *Visualization and Computer Graphics, IEEE Transactions on*, 1(4):328–342, 1995. doi:[10.1109/2945.485620](https://doi.org/10.1109/2945.485620).
- [14] Thomas Lewiner, Hélio Lopes, Antônio Wilson Vieira, and Geovan Tavares. Efficient implementation of marching cubes’ cases with topological guarantees. *Journal of Graphics Tools: JGT*, 8(2):1–15, 2003. doi:[10.1080/10867651.2003.10487582](https://doi.org/10.1080/10867651.2003.10487582).
- [15] W. Lorensen and H. Cline. Marching cubes: A high resolution 3D surface construction algorithm. *Computer Graphics*, 21(4):163–169, 1987. doi:[10.1145/37401.37422](https://doi.org/10.1145/37401.37422).

- [16] Chohong Min and Frédéric Gibou. Geometric integration over irregular domains with application to level-set methods. *Journal of Computational Physics*, 226(2):1432 – 1443, 2007. doi:[10.1016/j.jcp.2007.05.032](https://doi.org/10.1016/j.jcp.2007.05.032).
- [17] S. Osher and J.A. Sethian. Fronts propagating with curvature-dependent speed: algorithms based on Hamilton-Jacobi formulations. *J. Comput. Phys.*, 79(1):12–49, 1988. doi:[10.1016/0021-9991\(88\)90002-2](https://doi.org/10.1016/0021-9991(88)90002-2).
- [18] Charles S. Peskin. Numerical analysis of blood flow in the heart. *Journal of Computational Physics*, 25(3):220–252, November 1977. doi:[10.1016/0021-9991\(77\)90100-0](https://doi.org/10.1016/0021-9991(77)90100-0).
- [19] T. Strouboulis, K. Copps, and I. Babuška. The generalized finite element method. *Computer Methods in Applied Mechanics and Engineering*, 190(32-33):4081–4193, 2001. doi:[10.1016/S0045-7825\(01\)00188-8](https://doi.org/10.1016/S0045-7825(01)00188-8).